


 Cite this: *RSC Adv.*, 2018, **8**, 38745

Dendritic nanostructured FeS_2 -based high stability and capacity Li-ion cathodes†

Zhenxing Yu,^{abc} Junjie Wang,^a Na Zhang,^{de} Jungwoo Shin,^a Qiye Zheng,^a Subing Qu,^a Xiaoqing He,^a Angus Rockett,^a Hong Yang  ^{de} and Paul V. Braun  ^{a*}

Here we show that dendritic architectures are attractive as the basis of hierarchically structured battery electrodes. Dendritically structured FeS_2 , synthesized via simple thermal sulfidation of electrodeposited dendritic α -Fe, was formed into an electrode and cycled vs. lithium. The reversible capacities of the dendritic FeS_2 cathode were 560 mA h g^{-1} at 0.5C and 533 mA h g^{-1} at 1.0C after 50 cycles over 0.7 – 3.0 V. Over 0.7 – 2.4 V, where the electrode is more stable, the reversible capacities are 348 mA h g^{-1} at 0.2C and 179 mA h g^{-1} at 1.0C after 150 cycles. The good cycling performance and high specific capacities of the dendritic FeS_2 cathodes are attributed to the ability of a dendritic structure to provide good ion and electron conducting pathways, and a large surface area. Importantly, the dendritic structure appears capable of accommodating volume changes imposed by the lithiation and delithiation process. The presence of a $\text{Li}_{2-x}\text{FeS}_2$ phase is indicated for the first time by high-resolution transmission electron microscopy (HRTEM) and scanning transmission electron microscopy (STEM) electron energy loss spectroscopy (EELS). We suspect this phase is what enables electrochemical cycling to possess high reversibility over 0.7 – 2.4 V.

Received 12th September 2018
 Accepted 12th November 2018

DOI: 10.1039/c8ra07606e
rsc.li/rsc-advances

Introduction

In the quest for improved lithium-ion batteries (LIBs), considerable effort has been made to enhance the electrochemical properties of cathode materials.¹ Along with development of new material systems,^{2–5} an increasing number of groups are paying attention to the relationship between the electrochemical properties and the morphology of the active material.^{6,7} Nanostructuring offers a number of advantages, including shorter solid state ionic and electron transport pathways, and an increased contact area with the electrolyte, which improves the rate performance.^{8–11} However, this increased surface area can also lead to an increase in solid electrolyte interphase formation, which may be detrimental to the cycle life. Additionally, maintaining both good electron and ion transport pathways in a nanostructured system can be challenging.

^aDepartment of Materials Science and Engineering, Materials Research Laboratory, Beckman Institute for Advanced Science and Technology, University of Illinois at Urbana–Champaign, Urbana, Illinois 61801, USA. E-mail: pbraun@illinois.edu

^bBGRIMM Technology Group, Beijing 100160, China

^cBeijing Easpring Materials Technology CO., LTD, Beijing 100160, China

^dBeijing Aerospace Propulsion Institute, Beijing 100076, China

^eDepartment of Chemical and Biomolecular Engineering, University of Illinois at Urbana–Champaign, Urbana, Illinois 61801, USA

† Electronic supplementary information (ESI) available: Energy Dispersive Spectroscopy (EDS), more electrochemical tests (including electrochemical impedance spectroscopy (EIS), cycling performance tests and cyclic voltammetry (CV) tests) and high-resolution transmission electron microscopy (HRTEM) images are available. See DOI: 10.1039/c8ra07606e

It would provide a significant advantage if a hierarchical structure which exhibits a stable nanostructure and a robust macrostructure could be synthesized in a single step. Such a structure would provide a large number of active sites, a stable framework, and short diffusion lengths.^{12,13} Due to the advantages of such a structure, a wide range of hierarchically structured electrodes, which have exhibited excellent cycling performances and high reversible capacities, have been synthesized and studied,^{14,15} including hierarchical systems based on metal oxides,^{16–20} LiFePO_4 (ref. 21 and 22) and $\text{Li}_4\text{Ti}_5\text{O}_{12}$.²³ In cases such as Si, the hierarchical structure is also important in preventing volume change induced degradation during lithiation and delithiation.^{24,25} Notably, dendritic nanostructures, which have been widely studied in other fields, prior to this work, have not been considered for use as electrode materials for Li ion batteries.

Due to their high theoretical capacities, metal sulfides including SnS_x ,^{26–28} MoS_2 ,^{29–32} CuS_2 ,³³ and FeS_2 ,³⁴ CoS_2 ,³⁵ and Ni_3S_2 (ref. 36) are considered promising electrode materials. FeS_2 (pyrite) has in particular been commercialized as a lithium battery cathode due to its high theoretical capacity (894 mA h g^{-1}), earth abundance, environmentally benign nature and high temperature stability.^{37–40} With only a few exceptions however, pyrite has shown poor cyclability owing to its low electrical conductivity and limited reversibility, limiting its use to primary batteries.^{41,42} If these problems can be overcome, FeS_2 will be a much more promising cathode material for next generation lithium-ion batteries.



The pure iron pyrite nanowire cathode materials synthesized by Song *et al.*³⁸ retained a discharge capacity of 350 mA h g⁻¹ after 50 cycles and 0.1C, possibly because of the improved reaction kinetics provided by the nanostructure. Liu *et al.*³⁷ coated a carbon layer on octahedral FeS₂ nanocrystallites to enhance electrical conductivity and structure stability, and this system exhibited a capacity retention of 495 mA h g⁻¹ after 50 cycles at 0.5C. Wang *et al.*⁴³ reported hierarchically structured hollow FeS₂ microspheres which showed reasonable capacity and cycling performance (392.7 mA h g⁻¹ after 30 cycles at 1C). All of these works emphasized the importance of nanostructuring for improving the electrochemical properties of pyrite cathodes. Here, we describe a facile self-assembly route for preparing dendritically structured pyrite-based Li-ion cathodes. These dendritic FeS₂ composite cathodes exhibit high specific capacities and good cycling performance in the voltage window of both 0.7–2.4 V and 0.7–3.0 V. The Li_{2-x}FeS₂ phase was observed by high-resolution transmission electron microscopy (HRTEM) and electron energy loss spectroscopy (EELS) in scanning transmission electron microscopy (STEM) mode. Identification of this phase may enable further understanding of the lithiation/delithiation mechanism of FeS₂.

Experimental section

1 Synthesis of the hierarchically structured FeS₂

Ferrous sulfate heptahydrate (FeSO₄ · 7H₂O, Sigma Aldrich) was used to synthesize the dendritically structured α -Fe by an electric-field-induced and electrochemical reduction method.⁴⁴ The hierarchically structured dendritic pyrite was obtained *via* thermal sulfidation of the as-synthesized dendritic α -Fe at 450 °C for 4 hours with a heating and cooling rate of 15 °C per minute under a continuous argon gas flow. Elemental sulfur (99.5–100.5%, Sigma Aldrich) was placed at the edge of the furnace, where it reached about 140 °C and formed a melt. The resulting sulphur vapour was carried by the argon gas flow over the dendritic nanostructured α -Fe.

2 Material characterization

Sample composition and microstructure were determined by: X-ray diffraction (Philips X'pert XRD system with Cu K α radiation, $\lambda = 0.15418$ nm); scanning electron microscopy and energy dispersive spectroscopy (Hitachi S-4700 SEM, EDS); transmission electron microscopy and high-resolution transmission electron microscopy (JEOL 2100 cryo, TEM and HRTEM); and electron energy loss spectroscopy (EELS) during scanning transmission electron microscopy (JEOL, 2010F STEM). Cycling of TEM and STEM-EELS samples were performed by dispersing the dendritic nanostructured FeS₂ into ethanol, placing a couple of droplets on a copper grid with a carbon support film (EMS Acquisition Corp), covered by an identical copper grid and dried 2 h at 80 °C. The two grids were held by a toothless clamp and used as a cathode in a bottle cell. 1 M lithium hexafluorophosphate (LiPF₆) in a mixture of ethylene carbonate (EC), dimethyl carbonate (DMC) and diethyl carbonate (DEC) (2 : 1 : 2 in volume) was used as the electrolyte. 10 wt%

fluoroethylene carbonate (FEC, Sigma Aldrich) was added to the electrolyte. The counter electrode is lithium foil (Alfa Aesar). After 7 charge/discharge cycles using about 0.2C rates between 0.7–2.4 V, the samples were removed from the electrolyte, and immersed into dimethyl carbonate (DMC) solvent for 30 min to remove the rest of electrolyte. The copper grids were taken out of the glove box, and immediately transferred to the TEM column for analysis.

3 Fabrication of the composite cathode and electrochemical measurements

Composite electrodes were fabricated through mixing of the as-synthesized dendritic FeS₂, carbon black (Super P Conductive, Alfa Aesar), and poly(vinylidene fluoride) (PVDF, MTI) binder (65 : 25 : 15 weight ratio) using a homogenizer (GLH-115, OMNI International) for 15 min in *N*-methylpyrrolidone (NMP, MTI). The resulting slurry was printed onto a conductive carbon-coated copper foil current collector (MTI) with an average FeS₂ active material mass loading of 1–1.5 mg cm⁻². Then, the composite electrodes were dried for 10 h at 120 °C. 9.5 mm diameter electrode disks were punched and then dried at 100 °C in a vacuum oven for 12 h before cell assembly.

Two-electrode battery-type Swagelok cells were used to test the electrochemical properties of the composite electrode on a VMP3 (Bio-Logic) potentiostat. Cyclic voltammetry (CV) was performed between 0.7–2.4 V and 0.7–3.0 V at a scan rate of 0.2 mV s⁻¹. Electrochemical impedance spectroscopy (EIS) was performed on Swagelok cells after various cycle numbers at 2.4 V over a frequency range of 100 kHz to 10 mHz with an AC amplitude of 5.0 mV. The cells were kept at 2.4 V for 4 h, and allowed to rest for 4 h before taking EIS measurements.

Results and discussion

Fig. 1a–c shows scanning electron microscopy (SEM) images of the as-synthesized FeS₂. The dendritic FeS₂ particles are 8 to 15

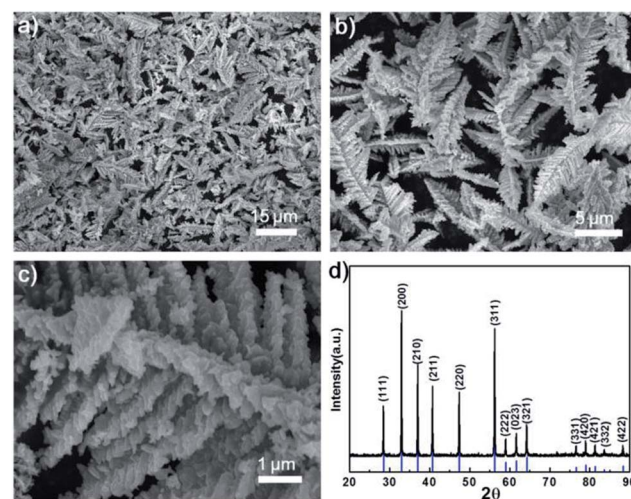


Fig. 1 (a) Low, (b) intermediate and (c) high magnification SEM images of dendritic nanostructured FeS₂; (d) XRD pattern of as-synthesized FeS₂ with JCPDS card 65-7643 included below the spectra.



μm in length and 4 to 6 μm in width, and possess a fine nanostructure on the branches and tips (in Fig. 1c). Energy dispersive spectroscopy (EDS) (Fig. S1†) indicates the atomic ratio of S to Fe is 2 : 1. All peaks in the X-ray diffraction (XRD) pattern (in Fig. 1d) can be indexed to pure cubic FeS₂ (JCPDS no. 65-7643, $a = 0.5404$ nm). No impurities such as elemental Fe, elemental S or marcasite were detected.

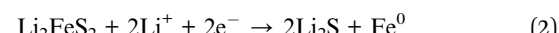
The electrochemical performance of as-synthesized dendritic nanostructured FeS₂ was studied in two-electrode battery-type Swagelok cells. The cycling and rate performance of the composite cathodes containing 60 wt% dendritic FeS₂ over the voltage range of 0.7–2.4 V and 0.7–3.0 V (in Fig. 2a and b) were investigated. Fig. 2a shows the cycling performance of the dendritic structural FeS₂ composite electrode between 0.7–2.4 V in an electrolyte with 10 wt% fluoroethylene carbonate (FEC) added. The specific capacities of the dendritic FeS₂ cathode are 566 mA h g⁻¹ (0.2C) and 449 mA h g⁻¹ (1.0C) in the 1st cycle, and 348 mA h g⁻¹ (0.2C) and 179 mA h g⁻¹ (1.0C) after 150 cycles, exceeding that reported for pyrite nano-wires over 0.7–2.4 V.³⁸

When cycling over 0.7–3.0 V, the specific capacities (in Fig. 2b) of a dendritic FeS₂ composite cathode could reach 796 mA h g⁻¹ (0.5C) and 717 mA h g⁻¹ (1.0C) after the 1st cycle, and 560 mA h g⁻¹ (0.5C) and 533 mA h g⁻¹ (1.0C) after 50 cycles, which is about 70% of the 2nd cycle capacity and superior to the performances of polyacrylonitrile (PNA)-FeS₂ (470 mA h g⁻¹ after 50 cycles at 0.1C)⁴⁵ and FeS₂ stabilization with a bis(trifluoromethanesulfonyl)imide (TFSI⁻) anion-based ionic liquid electrolyte over 1.0–3.0 V,³⁹ but lower than that of pyrite

nanocrystals (≥ 630 mA h g⁻¹) at the slow cycling rate of 200 mA g⁻¹.⁴⁶ Importantly, the dendritic FeS₂ cathodes always show a high coulombic efficiency (CE) for different C rates. The average CE after 5 cycles exceeded 99.5% for 0.7–2.4 V and 98.9% for 0.7–3.0 V, indicating a good electrochemical reversibility. The electrochemical performance of some FeS₂-based materials are shown in Table S1.† Fig. 2c shows voltage profiles between 0.7–2.4 V after the 10th cycle at each cycling rate. As the current density increases, the specific capacity decreases from 540 mA h g⁻¹ at 0.2C to 490 mA h g⁻¹, 400 mA h g⁻¹, 220 mA h g⁻¹ and 80 mA h g⁻¹ at 0.5C, 1C, 1.5C and 3C, respectively. Meanwhile, the conversion plateaus become gradually sloped and shorter due to voltage polarization at higher C rates. There is the same change trend for the conversion plateaus in the 0.7–3.0 V range as shown in Fig. 2d. The consecutive rate capability tests (in Fig. 2e and f) also present good cycling stability at each rate. The capacity recovers even after high C rate charge/discharge processes, indicating that high C rates did not damage the electrode.

Cyclic voltammetry (CV) curves of this composite cathode provide some information on the charge/discharge mechanism of FeS₂.

As shown in Fig. 3a and c, both CV curves show a broad reduction peak at approximately 1.2 V and a broad oxidation peak at about 2.0 V in the 1st cycle. This broad reduction peak has been suggested to correspond to the following reactions:⁴⁷



Due to the relatively slow diffusion of Li⁺ into FeS₂, reactions (1) and (2) proceed simultaneously at room temperature (≤ 30 °C), and thus only single broad reduction peak appears. The oxidation peak includes the reactions,^{45,48}

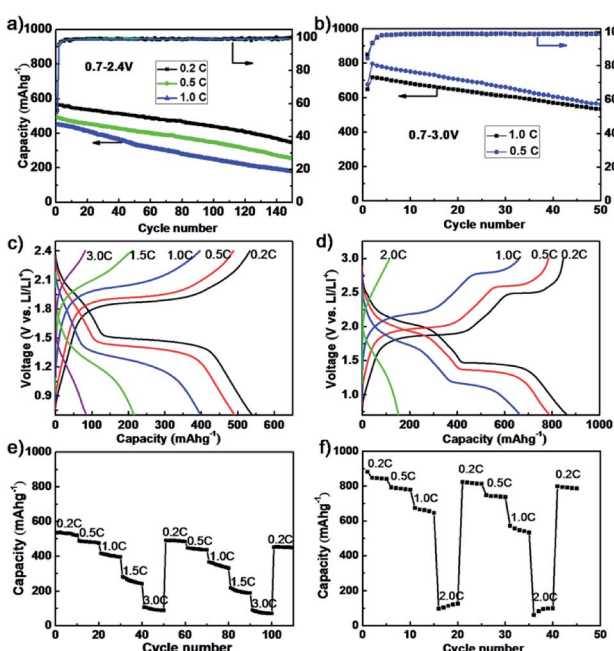


Fig. 2 Cycling stability of the dendritic FeS₂ composite electrodes (a) between 0.7–2.4 V at 0.2C, 0.5C and 1C, and (b) between 0.7–3.0 V at 0.5C and 1.0C; voltage–capacity curves in (c) 0.7–2.4 V and (d) 0.7–3.0 V range; and consecutive rate capability (e) from 0.2C to 3C over 0.7–2.4 V and (f) from 0.2C to 2C over 0.7–3.0 V.

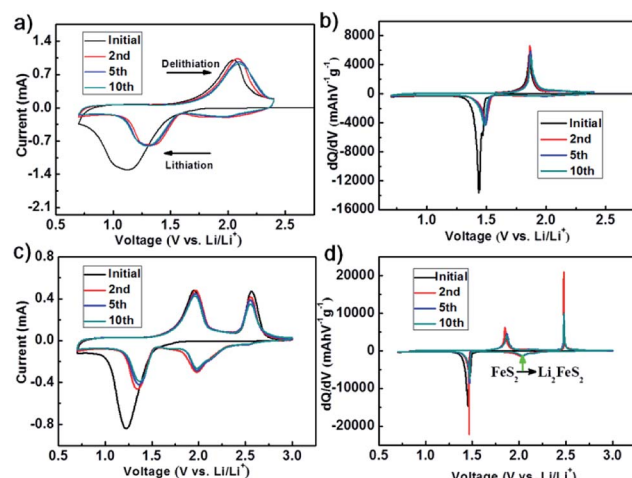
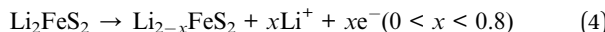
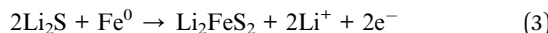
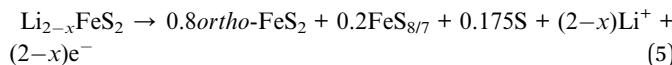


Fig. 3 Electrochemical properties of the dendritic FeS₂ composite cathode at different cycle. CV at a scan rate of 0.2 mV s⁻¹ over (a) 0.7–2.4 V and (c) 0.7–3.0 V; differential capacity versus voltage over (b) 0.7–2.4 V and (d) 0.7–3.0 V at 0.2C.





Generally, the hexagonal $\text{Li}_{2-x}\text{FeS}_2$ phase begins to decompose into *ortho*- FeS_2 above 2.4 V as described in reaction (5),^{38,48}



leading to another oxidation near 2.6 V (see Fig. 3c). Because the electrode does not fully revert to FeS_2 during oxidation, even above 2.4 V, the CE of the first few cycles is low.

After the first cycle, subsequent cycles between 0.7–2.4 V show a stable redox couple at 1.35 and 2.15 V corresponding to reactions (2), (3) and (4), respectively. The differential capacity *versus* voltage curves show that the redox reactions proceed at 1.50 and 1.85 V (Fig. 3b) when cycling at 0.2C. The CV curves of the composite cathode show two stable redox reactions during subsequent cycles when cycling over 0.7–3.0 V. In differential capacity curves (Fig. 3d), the peak at 2.50 V is from reaction (5), while the small broad reduction peak at 2.10 V corresponds to reduction of *ortho*- FeS_2 , S and lithium sulphides.⁴⁵ The S and lithium sulphides are difficult to decompose and dissolve more easily in the electrolyte, which lead to the low reversibility of reaction (5), and probably is the main reason for the rapid capacity fade during cycling between 0.7–3.0 V.^{38,49} A 3.0 V cut off voltage does provide greater capacity, but also results in fast capacity fade.

We suggest the FeS_2 electrochemical performance over 0.7–2.4 V can be attributed to the high reversibility of the intermediate $\text{Li}_{2-x}\text{FeS}_2$ and dendritic structure of FeS_2 which provides a large surface area,^{50,51} a good electron and ion transport network, and a mechanically robust structure (note, while we cannot extract the active material from a cycled electrode, as Fig. 4a shows, the dendritic structure is retained with cycling). The dendritic structure increases both the reaction area between the active materials and the electrolyte, and shortens the solid-state Li ion diffusion length. These are important parameters at high charge/discharge rates.

As result above, the dendritic nanostructured FeS_2 shows better cycling performance between 0.7 and 2.4 V than between 0.7 and 3.0 V, because of the high reversibility of the intermediate $\text{Li}_{2-x}\text{FeS}_2$ phase. To study the Li ion lithiation/delithiation process and confirm the formation of $\text{Li}_{2-x}\text{FeS}_2$, high-resolution transmission electron microscopy (HRTEM) images and scanning transmission electron microscopy energy loss spectroscopy (STEM-EELS) analyses in spot mode were performed on the dendritic FeS_2 after 7 cycles at low charge/discharge rates (about 0.2C). The voltage *vs.* time curve (in Fig. S2†) shows clear charging/discharging conversion plateaus. Fig. 4a shows TEM images of cycled dendritic FeS_2 , after the final charging to 2.4 V, indicating that the dendritic structure is retained after cycling. HRTEM images in Fig. 4b show a clear phase boundary on the edge of the dendritic FeS_2 . The majority of inner part of the sample shows a 0.271 nm lattice spacing, corresponding to (200) crystal planes of cubic FeS_2 . Another

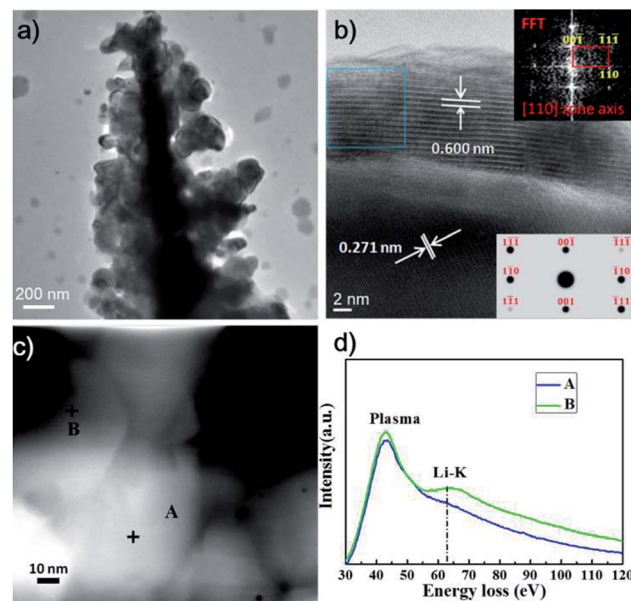


Fig. 4 (a) TEM, (b) HRTEM, and (c) STEM-HAADF images of the dendritic FeS_2 after 7 cycles at about 0.2C. (d) EELS spectra taken from the indicated regions in (c).

HRTEM image after cycling, as well as a HRTEM image before cycling tests is shown in Fig. S3.† These images indicate that after a small number of cycles, the inner parts of the dendrite are still cubic FeS_2 that has not reacted with Li. The lattice spacing near the surface is about 0.60 nm, very close to the theoretical value for the (001) planes in hexagonal-close-packed Li_2FeS_2 . The fast Fourier transform (FFT) of the image, shown in top right of Fig. 4b, was taken from the outlined regions in the image and can be indexed to the [110] zone axis of the Li_2FeS_2 phase (crystal data adopted from the International Crystal Structural Database (ICSD #68380)). A simulated electron diffraction pattern of the Li_2FeS_2 phase along the [110] zone axis using the CrystalMaker™ software (right bottom inset in Fig. 4b) is in good agreement with the experimental FFT pattern, suggesting that the outside layer of the structure is the Li_2FeS_2 phase. Due to the low cut off voltage of 0.7 V, lithiation is incomplete, and the material is likely to be $\text{Li}_{2-x}\text{FeS}_2$, which possess the same crystal structure as Li_2FeS_2 .

Fig. 4d shows the EELS spectra taken from the body (position A) and edge (position B) of cycled dendritic FeS_2 , as indicated in the STEM high angle annular dark field (HAADF) image in Fig. 4c. After background subtraction, a clear wide peak at about 63.5 eV is observed at the edge of cycled dendritic FeS_2 , which corresponds to the Li K-edge.⁵² The corresponding peak is not found in the intact inner region, indicating that only the outside part of dendrite is lithiated. Our TEM data provide direct evidence that the lithium ions are incorporated into the dendritic FeS_2 nanostructure, resulting in the formation of the $\text{Li}_{2-x}\text{FeS}_2$ phase during the lithiation process.

Besides of the high reversible intermediate $\text{Li}_{2-x}\text{FeS}_2$ phase, the robust dendritic structure is the other key factor of dendritic FeS_2 's good cycling properties. The architecture of FeS_2 provides



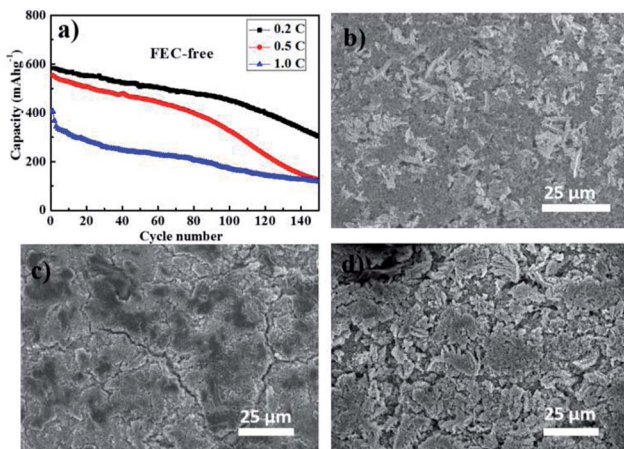


Fig. 5 (a) Cycling performances of the composite FeS_2 cathode in a FEC-free electrolyte at different C rates in 0.7–2.4 V range. SEM images of the dendritic FeS_2 composite cathode (b) before the cycling test, (c) after 150 cycles at 0.2C in FEC-free electrolyte and (d) after 150 cycles at 0.2C in 10 wt% FEC-containing electrolyte.

a large surface area, a good electron and ion transport network, and reduce losing of active materials during cycle process. In order to confirming the importance of dendritic structure, the cycling performance of dendritic FeS_2 composite cathode were tested in an electrolyte without FEC. The presence of FEC results in formation of a thin and stable SEI (Fig. S4 and Table S2†); which both enhances cycling reversibility, and appears to be an important contributor to retaining the dendritic structure of the electrode (Fig. 5). In a FEC-free electrolyte, the specific capacity of the dendritic FeS_2 cathode fades quickly, with the fall-off appearing to increase after about 100 cycles. After 150 cycles at 0.2C, the dendritic structure of FeS_2 appears considerably damaged (Fig. 5c) relative to the initial dendritic structure (Fig. 5b). In a 10 wt% FEC-containing electrolyte as already discussed, the dendritic FeS_2 composite cathode exhibits a much improved cycling performance (Fig. 2a). What we observe *via* SEM, is that the dendritic structure is retained in this case (Fig. 5d), a strong indication that the dendritic structure plays an important role in cycling performance.

Conclusions

We find that composite cathodes containing dendritic FeS_2 demonstrate good reversible capacity and stable cycling over 0.7–2.4 V, and an enhanced capacity but diminished cycling stability over 0.7–3.0 V. The reversible capacities of the dendritic FeS_2 cathodes were 560 mA h g^{-1} (0.5C) and 533 mA h g^{-1} (1.0C) after 50 cycles over 0.7–3.0 V, and 348 mA h g^{-1} (0.2C) after 150 cycles over 0.7–2.4 V. We propose that the reasonable cycling performance of the dendritic FeS_2 cathode at different C rates is due to the hierarchical structure, which shortens the Li^+ diffusion length and increases the contact area with the electrolyte in an architecture that is stable under volume changes due to lithiation and delithiation. The use of an FEC-containing electrolyte significantly improved the cycling performance,

presumably by resulting in a thin and dense SEI. However, we still observe a steady capacity fade, indicating probably that a more stable SEI is still required, and that a robust artificial SEI, for example such as one formed *via* atomic layer deposition, might be required to stabilize the dendritic structure over many cycles. We postulate that the $\text{Li}_{2-x}\text{FeS}_2$ phase, which was observed by HRTEM and STEM-EELS, is one reason that the dendritic FeS_2 shows better cycling performance over 0.7–2.4 V than over 0.7–3.0 V, where electrolyte-soluble products are formed.

Conflicts of interest

There are no conflicts to declare.

Acknowledgements

The authors acknowledge support of an AFOSR MURI (FA9550-12-1-0471) and experimental assistance from Dr Ke Sun and Dr Yang Hu. Z. Yu is grateful for fellowship support from the China Scholarship Council.

References

- 1 H. Li, Z. Wang, L. Chen and X. Huang, *Adv. Mater.*, 2009, **21**, 4593–4607.
- 2 P. L. Taberna, S. Mitra, P. Poizot, P. Simon and J. M. Tarascon, *Nat. Mater.*, 2006, **5**, 567–573.
- 3 H. Zhang, X. Yu and P. V. Braun, *Nat. Nanotechnol.*, 2011, **6**, 277–281.
- 4 Y. Xing, S. Wang, B. Fang, G. Song, D. P. Wilkinson and S. Zhang, *J. Power Sources*, 2018, **385**, 10–17.
- 5 Y. Xing, S. Wang, B. Fang, Y. Feng and S. Zhang, *Microporous Mesoporous Mater.*, 2018, **261**, 237–243.
- 6 P. G. Bruce, B. Scrosati and J.-M. Tarascon, *Angew. Chem., Int. Ed.*, 2008, **47**, 2930–2946.
- 7 K. Olszowska, J. Pang, P. S. Wrobel, L. Zhao, H. Q. Ta, Z. Liu, B. Trzebicka, A. Bachmatiuk and M. H. Rummeli, *Synth. Met.*, 2017, **234**, 53–85.
- 8 B. Kang and G. Ceder, *Nature*, 2009, **458**, 190–193.
- 9 A. S. Arico, P. Bruce, B. Scrosati, J.-M. Tarascon and W. van Schalkwijk, *Nat. Mater.*, 2005, **4**, 366–377.
- 10 C. Jiang, E. Hosono and H. Zhou, *Nano Today*, 2006, **1**, 28–33.
- 11 Y. Shao-Horn, S. Osmialowski and Q. C. Horn, *J. Electrochem. Soc.*, 2002, **149**, A1499–A1502.
- 12 Y.-G. Guo, J.-S. Hu and L.-J. Wan, *Adv. Mater.*, 2008, **20**, 2878–2887.
- 13 X. M. Yin, C. C. Li, M. Zhang, Q. Y. Hao, S. Liu, L. B. Chen and T. H. Wang, *J. Phys. Chem. C*, 2010, **114**, 8084–8088.
- 14 J. Jiang, Y. Li, J. Liu, X. Huang, C. Yuan and X. W. Lou, *Adv. Mater.*, 2012, **24**, 5166–5180.
- 15 J. Zai, K. Wang, Y. Su, X. Qian and J. Chen, *J. Power Sources*, 2011, **196**, 3650–3654.
- 16 L. Mai, L. Xu, C. Han, X. Xu, Y. Luo, S. Zhao and Y. Zhao, *Nano Lett.*, 2010, **10**, 4750–4755.
- 17 S. Gao, S. Yang, J. Shu, S. Zhang, Z. Li and K. Jiang, *J. Phys. Chem. C*, 2008, **112**, 19324–19328.



Open Access Article. Published on 19 November 2018. Downloaded on 2/8/2026 10:42:07 AM.
This article is licensed under a Creative Commons Attribution-NonCommercial 3.0 Unported Licence.

18 L.-Y. Jiang, X.-L. Wu, Y.-G. Guo and L.-J. Wan, *J. Phys. Chem. C*, 2009, **113**, 14213–14219.

19 J. S. Chen, Y. L. Tan, C. M. Li, Y. L. Cheah, D. Luan, S. Madhavi, F. Y. C. Boey, L. A. Archer and X. W. Lou, *J. Am. Chem. Soc.*, 2010, **132**, 6124–6130.

20 B. Wang, J. S. Chen, H. B. Wu, Z. Wang and X. W. Lou, *J. Am. Chem. Soc.*, 2011, **133**, 17146–17148.

21 H. Yang, X.-L. Wu, M.-H. Cao and Y.-G. Guo, *J. Phys. Chem. C*, 2009, **113**, 3345–3351.

22 C. M. Doherty, R. A. Caruso, B. M. Smarsly and C. J. Drummond, *Chem. Mater.*, 2009, **21**, 2895–2903.

23 L. Shen, C. Yuan, H. Luo, X. Zhang, K. Xu and Y. Xia, *J. Mater. Chem.*, 2010, **20**, 6998–7004.

24 A. Magasinski, P. Dixon, B. Hertzberg, A. Kvit, J. Ayala and G. Yushin, *Nat. Mater.*, 2010, **9**, 353–358.

25 Y. Zhao, X. Liu, H. Li, T. Zhai and H. Zhou, *Chem. Commun.*, 2012, **48**, 5079–5081.

26 Y. Li, J. P. Tu, X. H. Huang, H. M. Wu and Y. F. Yuan, *Electrochim. Acta*, 2006, **52**, 1383–1389.

27 S. Liu, X. Yin, L. Chen, Q. Li and T. Wang, *Solid State Sci.*, 2010, **12**, 712–718.

28 J.-W. Seo, J.-T. Jang, S.-W. Park, C. Kim, B. Park and J. Cheon, *Adv. Mater.*, 2008, **20**, 4269–4273.

29 L. Yang, S. Wang, J. Mao, J. Deng, Q. Gao, Y. Tang and O. G. Schmidt, *Adv. Mater.*, 2013, **25**, 1180–1184.

30 S. Ding, D. Zhang, J. S. Chen and X. W. Lou, *Nanoscale*, 2012, **4**, 95–98.

31 M. Wang, G. Li, H. Xu, Y. Qian and J. Yang, *ACS Appl. Mater. Interfaces*, 2013, **5**, 1003–1008.

32 H. Hwang, H. Kim and J. Cho, *Nano Lett.*, 2011, **11**, 4826–4830.

33 C.-H. Lai, K.-W. Huang, J.-H. Cheng, C.-Y. Lee, B.-J. Hwang and L.-J. Chen, *J. Mater. Chem.*, 2010, **20**, 6638–6645.

34 Y. Zhu, X. Fan, L. Suo, C. Luo, T. Gao and C. Wang, *ACS Nano*, 2016, **10**, 1529–1538.

35 Q. Wang, L. Jiao, Y. Han, H. Du, W. Peng, Q. Huan, D. Song, Y. Si, Y. Wang and H. Yuan, *J. Phys. Chem. C*, 2011, **115**, 8300–8304.

36 C.-H. Lai, K.-W. Huang, J.-H. Cheng, C.-Y. Lee, W.-F. Lee, C.-T. Huang, B.-J. Hwang and L.-J. Chen, *J. Mater. Chem.*, 2009, **19**, 7277–7283.

37 J. Liu, Y. Wen, Y. Wang, P. A. van Aken, J. Maier and Y. Yu, *Adv. Mater.*, 2014, **26**, 6025–6030.

38 L. Li, M. Caban-Acevedo, S. N. Girard and S. Jin, *Nanoscale*, 2014, **6**, 2112–2118.

39 T. Evans, D. M. Piper, S. C. Kim, S. S. Han, V. Bhat, K. H. Oh and S.-H. Lee, *Adv. Mater.*, 2014, **26**, 7386–7392.

40 Z. Tomczuk, B. Tani, N. C. Otto, M. F. Roche and D. R. Vissers, *J. Electrochem. Soc.*, 1982, **129**, 925–931.

41 D. Zhang, Y. J. Mai, J. Y. Xiang, X. H. Xia, Y. Q. Qiao and J. P. Tu, *J. Power Sources*, 2012, **217**, 229–235.

42 Y. Shao-Horn, S. Osmialowski and Q. C. Horn, *J. Electrochem. Soc.*, 2002, **149**, A1547–A1555.

43 Y. Wang, X. Qian, W. Zhou, H. Liao and S. Cheng, *RSC Adv.*, 2014, **4**, 36597–36602.

44 Z. Yu, Z. Yao, N. Zhang, Z. Wang, C. Li, X. Han, X. Wu and Z. Jiang, *J. Mater. Chem. A*, 2013, **1**, 4571–4576.

45 S.-B. Son, T. A. Yersak, D. M. Piper, S. C. Kim, C. S. Kang, J. S. Cho, S.-S. Suh, Y.-U. Kim, K. H. Oh and S.-H. Lee, *Adv. Energy Mater.*, 2014, **4**, 1300961.

46 M. Walter, T. Zund and M. V. Kovalenko, *Nanoscale*, 2015, **7**, 9158–9163.

47 S. K. Preto, Z. Tomczuk, S. von Winbush and M. F. Roche, *J. Electrochem. Soc.*, 1983, **130**, 264–273.

48 R. Fong, J. R. Dahn and C. H. W. Jones, *J. Electrochem. Soc.*, 1989, **136**, 3206–3210.

49 K. Kammer Hansen and K. West, *192nd International Meeting of The Electrochemical Society*, pp. 124–132.

50 Z. Yu, N. Zhang, Z. Yao, X. Han and Z. Jiang, *J. Mater. Chem. A*, 2013, **1**, 12462–12470.

51 Z. Yu, Z. Yao, N. Zhang and Z. Jiang, *RSC Adv.*, 2015, **5**, 25266–25272.

52 F. Wang, H.-C. Yu, M.-H. Chen, L. Wu, N. Pereira, K. Thornton, A. Van der Ven, Y. Zhu, G. G. Amatucci and J. Graetz, *Nat. Commun.*, 2012, **3**, 1201.

